Fiber and Integrated Optics, 24:149–169, 2005

ISSN: 0146-8030 print/1096-4681 online
DOI: 10.1080/01468030590922696

Taylor & Francis
Taylor & Francis Group

Photosensitive Materials for Integrated Optic Applications

P. V. S. MARQUES
P. J. MOREIRA

INESC Porto
Porto, Portugal, and
Universidade do Porto
Porto, Portugal

D. ALEXANDRE

INESC Porto
Porto, Portugal, and
Universidade de Trás-os-Montes
e Alto Douro
Quinta dos Prados
Vila Real, Portugal

M. MELO
T. E. A. SCHMIDT

INESC Porto
Porto, Portugal

R. MUENZNER

Alcatel SEL AG
Stuttgart, Germany

A. M. P. LEITE

Universidade do Porto
Porto, Portugal

J. S. AITCHISON

University of Toronto
Toronto, Ontario, Canada, and
University of Glasgow
Glasgow, Scotland

This article presents results of device fabrication using UV processing of materials and integrated optic components produced by flame hydrolysis deposition and hybrid sol-gel technology. Photosensitive materials were employed in the fabrication of channel waveguides and channel photo-imprinted waveguides incorporating Bragg gratings through single and double-step exposure.

Keywords integrated optics, flame hydrolysis, hybrid sol-gel, optical devices, photosensitivity, Bragg gratings, direct writing

Introduction

Integrated optical components based on a silicon platform have the potential to be a competitive solution for optical signal processing applications. Over the last decades, there has been extensive research directed to the development of materials and device

Received 30 October 2004.
Address correspondence to P. V. S. Marques, INESC Porto, Optoelectronics and Electronics Systems Unit, Rua do Campo Alegre, 687, Porto, 4169-007, Portugal. E-mail: psmarque@fc.up.pt

fabrication methods for the development of peformant integrated optic solutions. Among the technologies exploited, those related to silica-based materials are particularly relevant, of which flame hydrolysis and hybrid sol-gel techniques deserve particular attention.

The flame hydrolysis deposition technique is a vapor delivery method developed to synthesize high-purity fine silica particles through a hydrolysis process in a high-temperature flame, using an oxy-hydrogen torch. Kawachi et al. [1] were the first to apply flame hydrolysis deposition (FHD) to the realization of planar lightwave circuits (PLCs) due to its high throughput, excellent doped silica quality, and versatility in terms of doping species. Since this first work, numerous results have been published confirming FHD, in conjunction with reactive ion etching (RIE), as a very performant technique for PLC production. In addition, the FHD process has been used to fabricate lanthanide-doped waveguide lasers and amplifiers in silica [2].

The hybrid sol-gel process is a promising route for production of low-cost organic–inorganic, glass-based integrated optical devices, as it offers the advantage of low-temperature fabrication and does not require sophisticated equipment [3]. The presence of the organic components increases the flexibility of the gel network, preventing its cracking, permitting low consolidation temperatures, and opening the possibility to combine the attractive features of organic polymers with those of a silicate network at the molecular level. Adequate choice of an organic polymeric group allows the definition of microstructures, such as channel waveguides, using simple, low-cost photopolymerization as an alternative to the complex dry-etching procedure used with purely inorganic glass [4].

One property that can be an attribute to materials produced via the two synthesis techniques referred above is photosensitivity, which has been exploited in the fabrication of fiber and planar devices, an effort stimulated by the extremely important role of the resulting devices in optical communication and sensing systems. It should, however, be emphasized that in the case of inorganic materials the photosensitivity is mainly due to oxygen defect centers [5], while in hybrid sol-gel materials the refractive index changes arise from a structural change of the organic component [6].

In the case of purely inorganic materials such as those produced by FHD, the photosensitivity effect has been used primarily to produce in-core Bragg gratings using the permanent index change obtained under UV exposure [7, 8]. The same effect can also be usefully employed in UV trimming of devices [9, 10] and in direct writing of 2-D components, such as directional couplers [11, 12] and power splitters [12]. Direct writing is particularly attractive since it avoids recourse to expensive and time-consuming RIE in defining the waveguide structures. Attention is, therefore, beginning to focus on the use of photosensitivity as a method for transferring the waveguide device pattern into the silica glass.

In the case of the hybrid material synthesized from the precursor methacryloxypropyltrimethoxysilane (MAPTMS), the organic groups contain unsaturated C=C double bonds, so they can be photopolymerized by ultraviolet (UV) radiation exposure [6], thus becoming resistant to organic solvents, whereas the unexposed material can be simply dissolved away by a suitable organic solvent [13]. The addition of photoinitiators in the final preparation step of the sol-gel solution, such as Irgacure 184 or 1800 (CIBA) or hydroxymethylpropiophenone (HMPP), has been employed [14, 15]. Therefore, the photosensitive properties of this class of materials allow the fabrication of integrated devices without recourse to RIE.

In this article, the production of integrated devices employing photosensitivity as an essential characteristic for the device fabrication routine is described. In the case of materials produced by FHD, the fabrication of Bragg gratings in etched waveguides

is reported, followed by the explanation of direct writing experiments that allow the fabrication of devices without reactive ion-etching processes. In the case of hybrid materials, tridimensional waveguide fabrication through photo-polymerization and dissolution is described in detail. Simultaneous photo-imprinting of a straight waveguide with a Bragg grating incorporated in its central section is reported for both inorganic and hybrid materials.

Experiments

The FHD Synthesis Route

The Deposition System. The FHD system assembled at Glasgow University, which was used to partially produce the samples used on this work [16], incorporates a reagents cabinet, which consists of a sealed glove box that contains the bubbler bottles with their respective reagents ($SiCl_4$, $POCl_3$, and $GeCl_4$), a deposition chamber, and a waste scrubber. The final glass composition is determined by the carrier gas (N_2) flow to each reagent bottle, which is regulated through high-precision mass flow controllers (MFCs). Since this method relies on a vapor delivery technique, the reagents are kept at constant temperature (by silicone oil circulating in a closed circuit in the outer jacket of their respective reagent Drechels bottles) in order to ensure a good process control. BCl_3 was already supplied as a gas and therefore used a separated delivery line.

The hydrolysis reaction takes place in the closed deposition chamber (at atmospheric pressure), which houses the circular turntable where the substrates are placed and the oxy-hydrogen torch. Two computer-controlled stepper motors are assembled underneath the chamber, one used for turntable rotation and the other for the linear movement of the arm that holds the torch. The final thickness of the glass layer deposited is determined by the combined movements of rotation of the turntable and linear displacement of the torch above the substrates. A local exhaust is placed above the turntable surface in order to ensure an efficient removal of corrosive reaction products and unreacted reagents.

Calibration of the FHD system was first conducted using planar waveguides produced on oxidized silicon wafers. The most important characteristics to be determined are the thickness and the refractive index of the slab layer versus dopants concentration, as well as the optimal sintering conditions required to achieve defect-free glass layers. Several fabrication parameters were investigated, such as reagent flow, flame and turntable temperature, torch position, and sintering parameters (dwell temperature and time, temperature ramps, and sintering environment). In all cases the flame was fed with constant flow rates for $SiCl_4$ (150 cm^3/min) and BCl_3 (65 cm^3/min), while the $GeCl_4$ flow rate was adjusted in order to control the refractive index difference to the thermal silicon oxide layer. Flame fueling was ensured by constant flows of O_2 (5 L/min) and H_2 (7 L/min), as a more efficient incorporation of germanium was found with high-temperature flames, probably due to better reaction efficiency. The samples were sintered in a tubular furnace in a helium-rich environment, produced by a constant helium flow of 0.6 L/min. The sintering temperature was approximately 1325°C for a dwell time of 2.5 h. The samples were inserted and removed at approximately 850°C and the ramping rates employed were 15°C/min. As an example of the characterization of the fabrication procedure, Figure 1 shows the results of the refractive index as a function of the $GeCl_4$ flow rate, which are relevant for the proper deposition of waveguide core layers. The refractive index of the planar layer was measured using the m-lines technique. The parameters employed resulted in a final layer thickness of 1.0 ± 0.1 μm per pass of the torch.

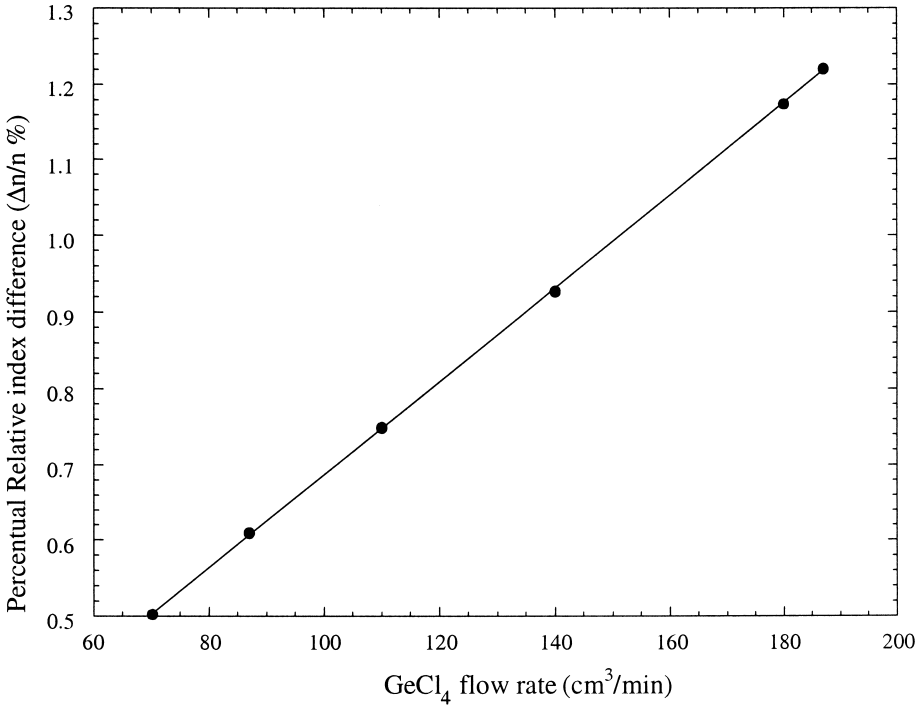

Figure 1. Flame hydrolysis deposition system calibration for germano-borosilicate glass. The $SiCl_4$ and BCl_3 flow rates were 150 and 65 cm^3/min, respectively. The oxygen and hydrogen flow rates were 7 and 5 L/min, respectively.

Photosensitivity Assessment and Device Fabrication

Bragg gratings. Following FHD system calibration, the photosensitive response of germanium-boron–doped silica layers was assessed as deposited and after photosensitivity enhancement (either through cold hydrogenation or flame brushing).

The refractive index changes in planar waveguides due to UV exposure were determined by protecting half of the sample while uniformly exposing the other half. The changes were determined by comparing the refractive index of both areas, as given by the prism coupler and m-lines technique. The saturation values for index change in planar waveguides (core thickness of 6 μm and relative refractive index difference of $\frac{\Delta n}{n} = 0.75\%$) due to UV exposure, using a KrF excimer laser operating at 248 nm, were 5×10^{-4} for as-grown samples and 4×10^{-3} for flame-brushed samples (due to the absence of a cladding layer, flame brushing employing an oxy-hydrogen torch [17] was used as the photo-sensitization method, since flame brushing induces permanent hydrogenation as opposed to "cold" hydrogenation at high pressure, where molecular hydrogen will rapidly diffuse out). In addition, Bragg gratings were written into standard channel waveguides defined by reactive ion etching and buried using a cladding layer, with the refractive index matching that of the thermal silicon dioxide buffer. Gratings were photo-imprinted using the conventional phase mask approach. The transmission spectrum evolution due to UV exposure through a 6-mm-long phase mask (period of 1060 nm) in an etched waveguide with a relative refractive index contrast to the thermal buffer layer of 0.75% and core dimensions of 6×6 μm^2 can be seen in Figure 2. The samples were

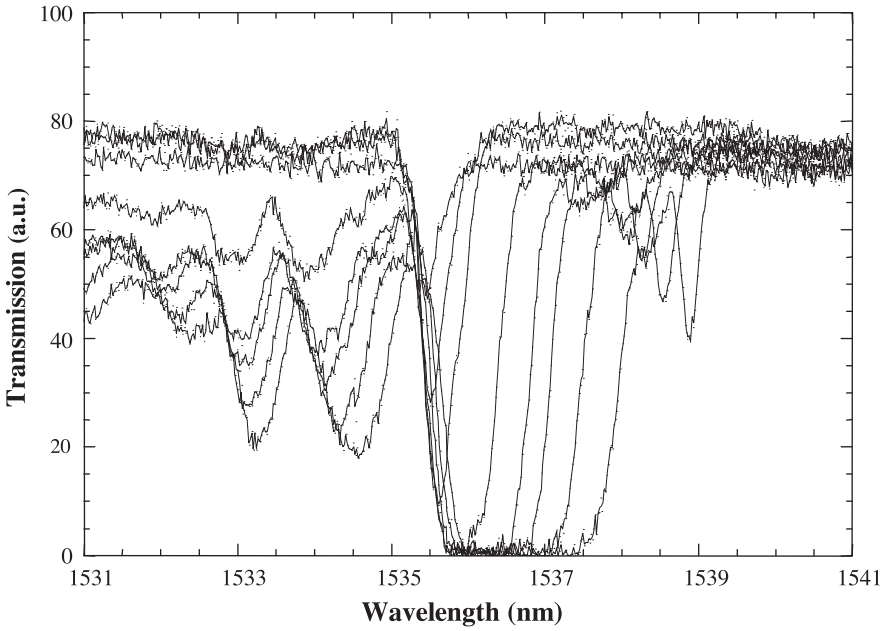

Figure 2. Evolution of the Bragg grating transmission spectrum with UV exposure (200 mJ/cm^2 per pulse at 20 Hz). The narrowest and the broadest spectra were obtained with 4500 and 35,000 pulses, respectively.

hydrogen loaded prior to UV exposure for $\sim$2 weeks in a high-pressure chamber (120 atm, room temperature). Analysis of the evolution of the grating spectral characteristics shows that the central Bragg wavelength moves toward longer wavelengths as the exposure proceeds, due to an increase of the average core refractive index. Simultaneously, there is an increase of the grating bandwidth and side features start to develop as the exposure progresses toward saturation. There is a characteristic rise in coupling to higher-order modes that reflects itself on a drop in transmission at wavelengths shorter than the central Bragg wavelength. The peak that develops at a longer wavelength is attributed to e-beam writing stitching errors in the phase mask used.

Figure 3 shows the evolution of the maximum grating reflectivity as a function of the UV exposure; this behavior is characteristic of germanium-doped silica, which exhibits a positive refractive index change due to exposure. The refractive index change estimated from the results of Figures 2 and 3 is a rise of at least 3.6×10^{-3}.

Integrated lasers. Intra-core Bragg gratings offer an elegant solution to form the laser cavity in comparison with dielectric mirrors butt-coupled or directly deposited on the waveguide ends. The fabrication of a monolithic laser configuration requires a successful combination of a material capable of UV photo-imprinting of Bragg gratings with a host with high solubility of lanthanide ions, both properties being closely related to the core dopants employed. Phosphorous is a suitable co-dopant to achieve high lanthanide concentration, but adversely reduces the UV absorption bands at the most commonly employed UV writing wavelengths. Germanium has the opposite characteristics regarding photosensitivity/solubility. The demonstrated laser configuration is based on a waveguide core that combines two layers produced by FHD, with the same refractive index but with different doping characteristics: one exhibits high photosensitivity, while the other

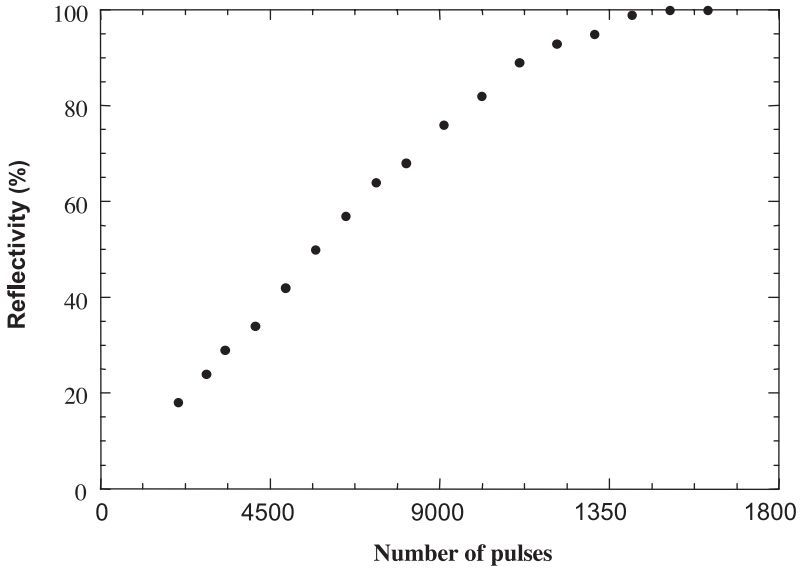

Figure 3. Evolution of peak reflectivity for the grating characterized in Figure 2.

has high lanthanide solubility. A schematic representation of the structure fabricated is represented in Figure 4.

The waveguides were also fabricated by flame hydrolysis deposition and reactive ion etching. Initially, a 2-μm photosensitive layer was deposited on top of a 15-μm-thick pure oxide undercladding, obtained by silicon oxidation. This photosensitive layer was doped with germanium and boron. A second core layer, 4-μm thick, was then deposited and consolidated. This layer was doped with neodymium and used a phosphorous/aluminum-based silica host, produced by aerosol doping techniques [18]. The Nd^{3+} concentration is estimated to be $\approx$0.21 wt% by comparison with measured samples produced under similar conditions [18]. The core ridges were formed by photolithographic processes and RIE and covered with an overcladding layer with the refractive index matching that of the thermal oxide buffer. The total core thickness is 6 μm and the relative index difference to the adjacent layers is 0.75% (the two core layers were index matched). The total sample length is 5 cm.

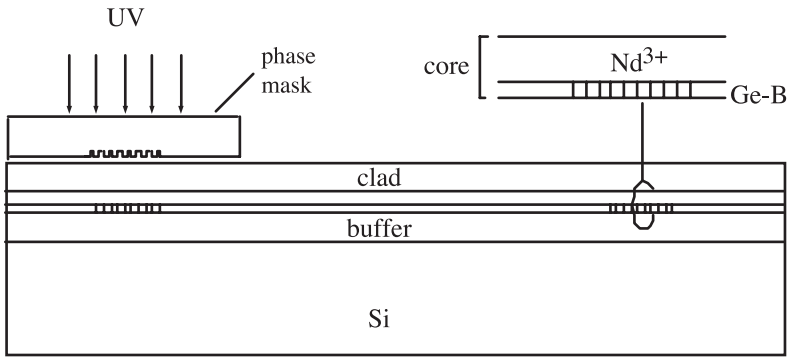

Figure 4. Schematic representation of the laser structure.

The laser cavity was defined by two Bragg gratings, fabricated by UV exposure to a KrF excimer laser (248 nm) through a fused silica phase mask, as represented in Figure 4. To enhance the photosensitivity response, the samples were hydrogenated for 2 weeks at 100 atm (room temperature). The 8-mm-long Bragg gratings were monitored during the UV exposure using a white light source and an optical spectrum analyzer. Due to a smaller overlap between the optical mode distribution and the photosensitive layer in comparison with a uniform Ge-doped core, the gratings reached saturation at around 80% reflectivity and had a bandwidth of about 0.8 nm. The distance between gratings was 25 mm, corresponding to a free spectral range of about 4.1 GHz (0.015 nm). Since the active layer was doped with neodymium, the Bragg wavelength was situated near the peak of the fluorescence band, centered at 1053 nm.

Figure 5 shows the output spectrum recorded with an optical spectrum analyzer for a $8\times6\ \mu m^2$ core section waveguide pumped at 802 nm using a Ti:Sapphire laser. The threshold for laser action was 93 mW (estimated coupled pump power, determined by taking into account non-absorbed pump power, Fresnel, coupling, and scattering losses), and a slope efficiency of 0.3% was obtained as demonstrated in Figure 6. Since the gratings are expected to be similar, the total efficiency should be approximately 0.6%. In Figure 7, the result of a Fabry-Perot scan is represented, demonstrating single longitudinal mode operation. Monomode operation is thought to be due to the combined effects of slightly shifted gratings and laser cavity mode spacing.

Channel waveguide writing. The refractive index change usually achievable is sufficient to attain 2-D confinement, and therefore functional devices can be fabricated without recourse to dry-etching processing stages. In order to evaluate the capability of writing channel waveguides, the layered planar structure shown in Figure 8 was employed. The central photosensitive layer, doped with germanium and boron, had a thickness $d_1 = 6\ \mu m$

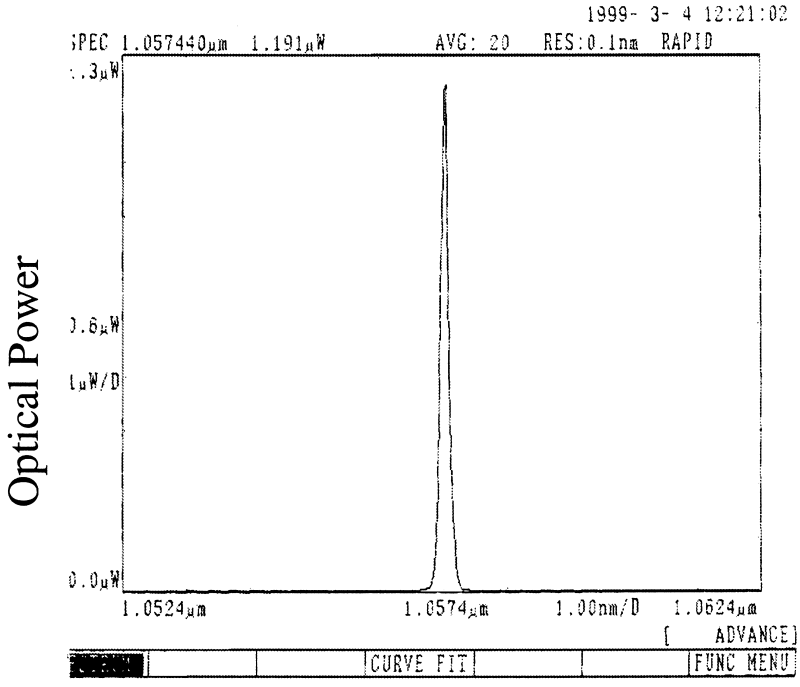

Figure 5. Laser output spectrum for a pump power of 200 mW (waveguide core section $8\times6\ \mu m^2$).

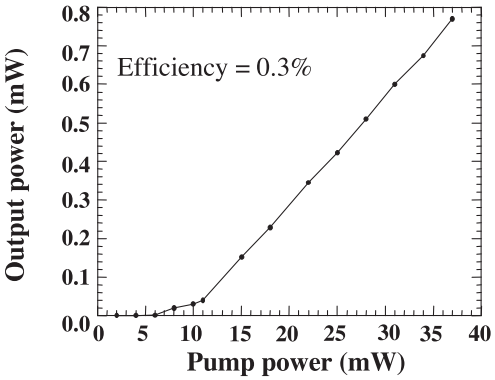

Figure 6. Laser output power as a function of estimated coupled pump power (waveguide core section $8 \times 6\ \mu m^2$).

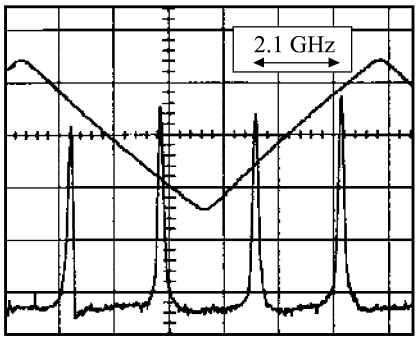

Figure 7. Fabry-Perot scan of the waveguide laser emission, using a free spectral range of 2.1 GHz.

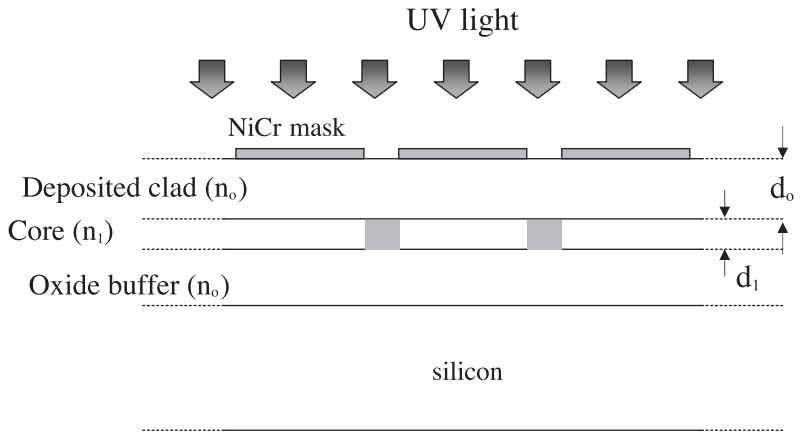

Figure 8. Schematic representation of the cross-section structure of the samples used for direct writing experiments.

and a relative index difference of 0.9% with respect to the thermal oxide lower cladding. The phosphorous- and boron-doped cladding thickness was $d_o = 15$ μm thick and its refractive index matched that of the buffer layer; this cover layer was designed to be transparent at the writing wavelength, and its thickness was chosen to simultaneously permit a reasonable hydrogen retention time after removal from the hydrogenation chamber and avoid serious mask diffraction effects as reported in [7]. The nichrome amplitude mask was fabricated with standard photolithography and nichrome wet-etching. In another approach, masks were defined on UV-grade silica plates, which were put in contact with the sample surface, with the mask facing down. This would in principle reduce the fabrication time, since a single mask could be used for more than one sample, but the method is more sensitive to mechanical vibrations (which are minimized by pressing down the mask against the sample with strong clamps specially designed to the effect). The devices were treated with the same hydrogenation routine as the samples used for grating tests. The top view of a set of straight waveguides defined by direct writing is shown in Figure 9. Diffraction effects are not to be seen, and the waveguide dimensions clearly reproduce quite well the mask widths.

One negative aspect is that the metallic mask can be damaged by the UV exposure. The threshold for damage was determined to be approximately 300 mJ/cm^2 per pulse at 30 Hz for masks on transparent silica plates; in the case of nichrome masks deposited on the sample surface, the threshold for mask damage seemed to be smaller. In the former case, UV radiation hits the mask interface in contact with the fused silica, which is obviously very clean and non-oxidized. In the case of NiCr layers deposited on the sample surface, the UV light exposes the surface layers that are not so clean (exposed to the air) and probably oxidized, and this is possibly a cause for the lower threshold for damage. In Figure 10, the photograph of a sample (top view) with severe NiCr damage is presented for illustration.

One problem associated with direct writing in planar layers that are non-matched in terms of refractive index values is due to the fact that the optical mode is asymmetric

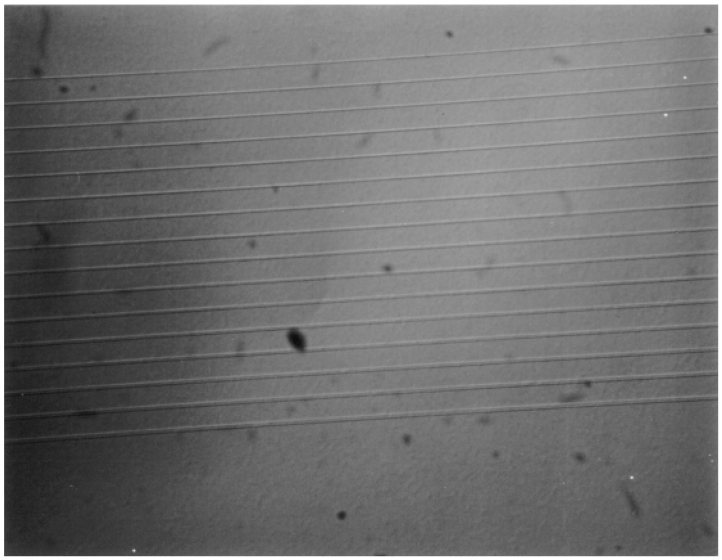

Figure 9. Top view of a set of directly written straight waveguides with widths ranging from 3 to 18 μm (250 mJ/cm^2 per pulse, 25 Hz, 15 min).

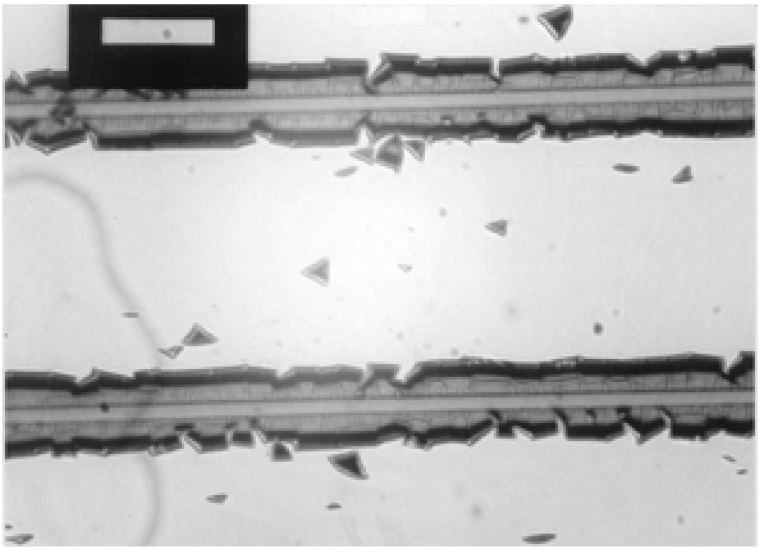

Figure 10. Damage of the mask defined on an 80-nm-thick NiCr layer deposited on the sample (325 mJ/cm^2 per pulse, 30 Hz, 15 min).

(leading to higher coupling losses) [19] and that for strong UV-induced refractive index changes, the UV written waveguide becomes multimode. These problems can be overcome by the use of an index-matched layer structure. Figure 11 allows a comparison of the cross-section of UV-written waveguides in matched and non-matched planar layer structures, whereas Figure 12 displays the cross-sections of etched and UV-written waveguides in index-matched structures.

Channel waveguide Bragg gratings. The use of photosensitivity to obtain optical guidance by refractive index modification, together with a superimposed refractive index modulation to form a Bragg waveguide grating, was investigated.

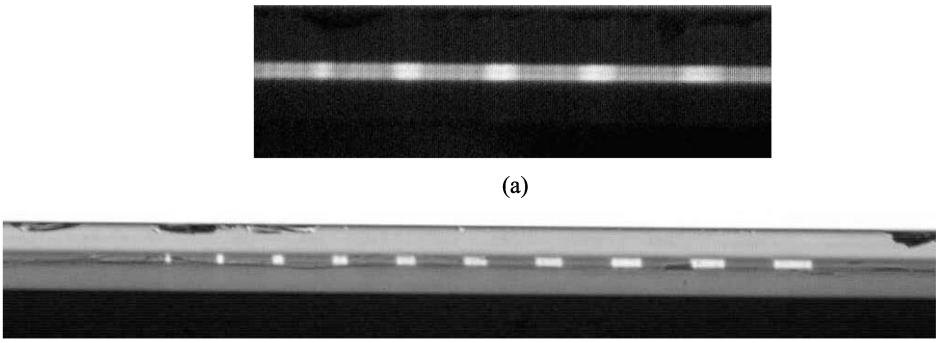

(a)

(b)

Figure 11. Cross section of UV direct written waveguides in (a) non-index–matched structures and (b) index-matched structures. Parameters are (a) $n_{core} = 1.4608$, $n_{buffer} = 1.4456$, $n_{clad} = 1.4458$, photosensitive layer thickness $= 4.6$ μm, clad thickness $= 19.9$ μm; and (b) $n_{core} = 1.4458$, $n_{buffer} = 1.4457$, $n_{clad} = 1.4460$, photosensitive layer thickness $= 4.2$ μm, clad thickness $=$ 15.2 μm (all refractive index values at 1.55 μm).

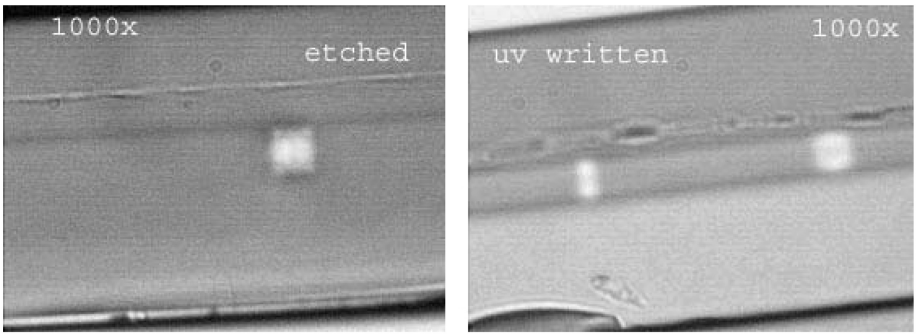

Figure 12. Comparison between an etched waveguide and a UV-written waveguide defined in an index-matched layer structure. The data for the UV-written sample (index matched) is the same as for Figure 11.

In a first approach the sample surface was coated with an 80-nm-thick film of nichrome, and lines with widths ranging from 3 to 10 μm were defined in the nichrome mask. Exposure proceeded in two steps; in the first, the sample was evenly exposed, through the mask, to the UV beam, without phase mask (7 minutes, 20 Hz, 200 mJ/cm^2 per pulse), for definition of a homogeneous "background" waveguide, and care was taken in order to ensure that some photosensitivity margin was left. A second exposure step was then performed through a phase mask aligned with the amplitude mask to define a Bragg grating in the channel waveguide "pre-defined" in the first exposure (additional 12 minutes exposure, 20 Hz, 200 mJ/cm^2 per pulse). The result is shown in Figure 13, which corresponds to a $\sim$80% reflectivity grating in a single-mode waveguide. The central Bragg wavelength shifted to longer wavelengths in this case, because the effective index in directly written waveguides was higher than in the etched waveguides referred above. The short wavelength resonances recorded in this case can also be due to a nonuniform UV exposure. This situation usually results in a non-constant average refractive index along the grating length that leads to a symmetrically chirped Bragg grating, causing Fabry-Perot interference effects to develop in the transmission spectrum.

The exposure time for each exposure step was roughly calculated from the growth dynamics shown in Figure 3, and the objective was to attain a 100% reflectivity grating after the second exposure. Several factors can be responsible for the lower reflectivity achieved, the most probable being a different growth dynamics from that of Figure 3, which was obtained for samples with different GeO_2 concentration.

The refractive index change was, in this case, extrapolated from the position of the central Bragg wavelength. Calculations were performed for a 6×6 μm^2 core with a refractive index $n^{core} + \Delta n^{UV}$. For $\lambda_B = 1545$ nm, the refractive index change was calculated to be $\Delta n^{UV} \sim 6 \times 10^{-3}$ (for a relative index difference of the photosensitive layer to the adjacent layers of 0.9%). The insertion loss measured in the same waveguide was 4.5 dB, using single-mode fibers (mode field diameter of 10.5 μm at $1/e$). The calculated coupling loss was approximately 2 dB per end-facet, and thus the estimated propagation loss was 0.5 dB/cm.

A very positive aspect of simultaneous writing of waveguide plus grating is that from the central Bragg wavelength (which is directly related to the modal effective index constant) and from the waveguide dimensions, it is possible to accurately extract the UV-induced refractive index simply by employing the effective index method. A negative point in this approach is a more pronounced occurrence of damage in the nichrome mask

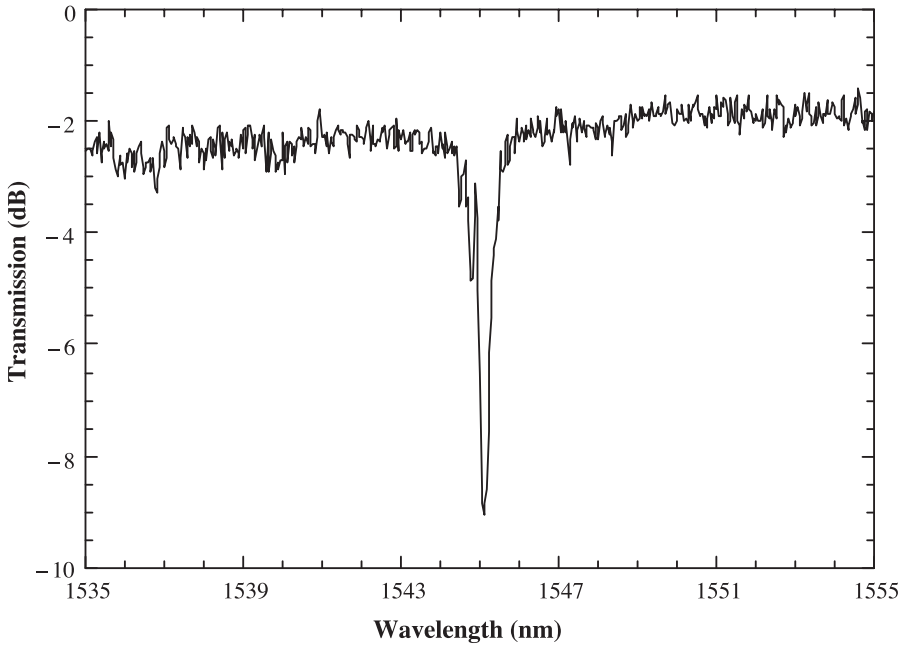

Figure 13. Transmission spectrum of a directly written linear waveguide with a Bragg grating obtained under simultaneous UV exposure.

in zones exposed through the phase mask. The fluence increases at locations of construtive interference, and hence the threshold, as measured in the free beam, is reduced, but this fact was not considered in the calculation of the UV fluence level.

The final approach involved the definition of a channel waveguide containing a Bragg grating by using a combined amplitude and phase mask (Figure 14) and a single exposure step. In this case the phase mask was covered with a thin metallic layer and the transparent lines were defined through the phase mask region and aligned perpendicular to the phase mask grooves. Figure 15 shows the transmission spectrum of a waveguide containing a Bragg grating in its central part. One negative point of this approach is that it is difficult to monitor the waveguide/grating growth in real time. A top view of the waveguides, Figure 16, shows clearly that the waveguide is not so well defined in the border region of the section containing the Bragg grating. This effect is due to the fact that there is a narrow end region where only one of the phase mask diffraction orders exposes the sample. The extent of this region depends on the thickness of the cladding and on the angle of the ± 1 diffraction orders; for the phase mask used it is of about 5 μm large. No problems have been associated with this feature, either in terms of insertion loss or grating spectral properties.

The Hybrid Sol-Gel Synthesis Route

The production of integrated devices employing the hybrid sol-gel technique involves the synthesis of core, buffer, and cladding material layers and device pattern definition through UV exposure, followed by dissolution of non-exposed areas [13].

The ideal sol-gel material for the buffer layer should possess the following characteristics: 1) low refractive index; 2) allow crack-free thick film ($\sim$10 μm) deposition in a

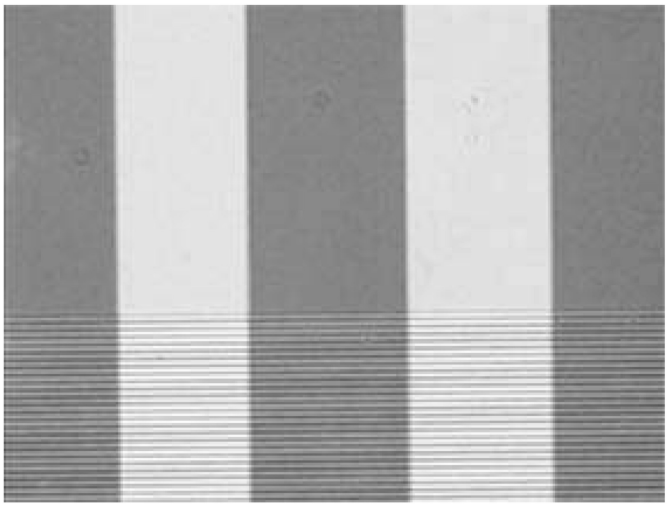

Figure 14. Microphotograph of a combined phase and amplitude mask for simultaneous direct writing of a waveguide containing a Bragg grating.

single step; 3) low optical loss; and 4) low material cost. The solution to achieve crack-free thick films consists of employing a material with low network connectivity. This can be accomplished by the choice of a di-functional monomer where the non-hydrolyzable organic group does not form covalent bonds with the neighbor molecules. Apparently, the refractive index of the material is associated with the linear chain dimension of the organic group present in the hybrid material; usually, materials with larger organic

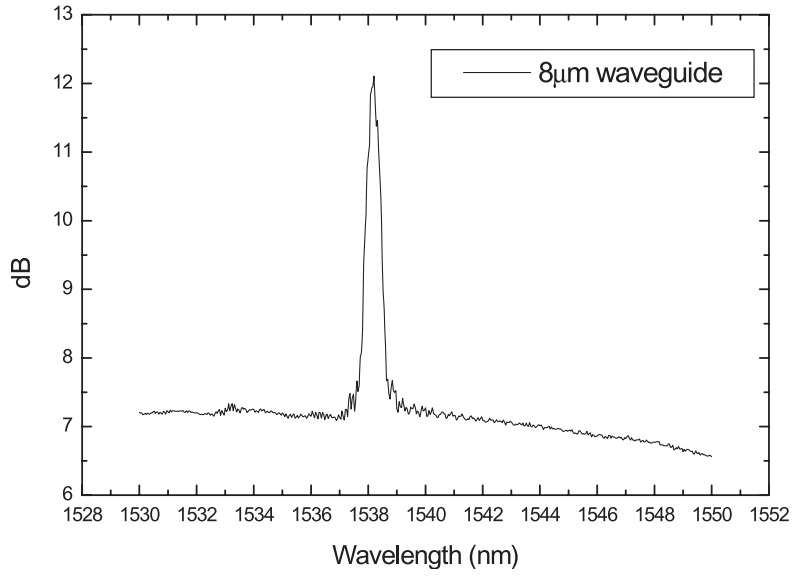

Figure 15. Reflexion spectrum of a Bragg grating in a UV-written waveguide fabricated through a process of simultaneous writing.

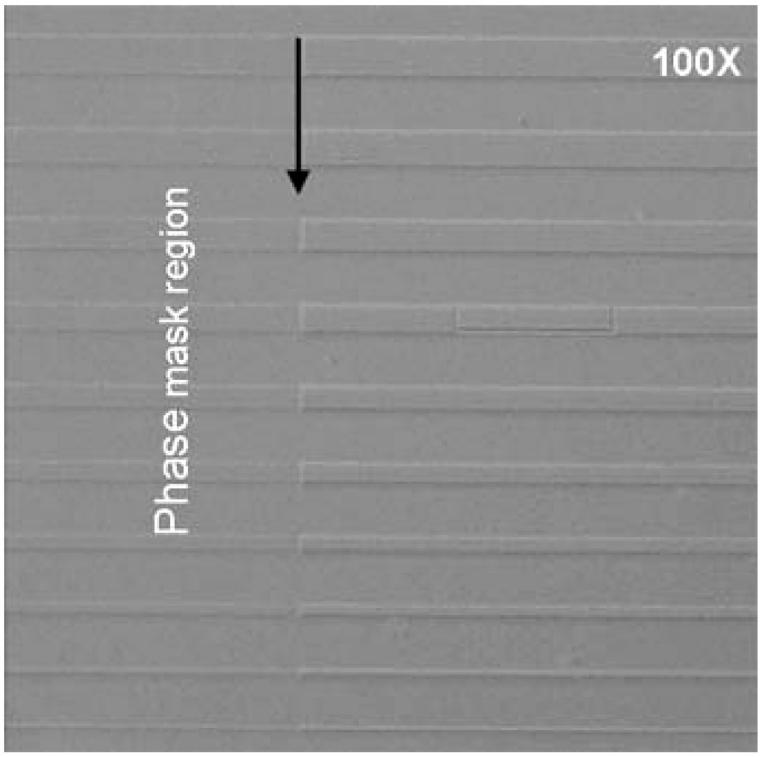

Figure 16. Top view of waveguides exposed to the combined phase and amplitude mask of Figure 14. The arrow indicates the border of the phase mask region.

groups have a higher refractive index. So, the starting option is the choice of the short methyl group ($-CH_3$) for the organic component; corresponding di-functional precursors are dimethyldimethoxysilane (DMDMOS) or dimethyldiethoxysilane (DMDEOS). Although DMDMOS is more expensive than DMDEOS, in the experiments performed it was preferred over DMDEOS as the methoxide groups react faster than the ethoxide groups in the hydrolysis reaction, and thus the preparation time of the sol is reduced. DMDMOS was combined with tetramethoxysilane (TMOS) with different molar ratios TMOS:DMDMOS of x:1, where $x = 0.5$, 0.7, 0.8, 0.9, 1.0 were experimented. Among the possible solutions, the TMOS/DMDMOS system with a molar ratio of 0.8:1 presented the best results concerning homogeneity and surface uniformity of the films. This composition was thus chosen for fabrication of buffer/cladding layers.

Hydrolysis and condensation was performed by mixing acidified water (0.1 M HCl) and the sols were stirred in a sealed container for a few hours until reaching the necessary viscosity to produce spin-coated thick films ($\sim$10 μm or above). The total water quantity was calculated attending to the specific combination ratio of the alkoxides employed and to their respective partial water:alkoxide molar ratios; molar ratios of 2:1 for tetraalkoxide (TMOS), 1.5:1 for trialkoxide (MTMOS), and 1:1 for dialkoxide (DMDMOS) were employed.

The buffer/cladding layers were deposited at 800 rpm by spin-coating on soda-lime glass substrates previously cleaned using a standard cleaning sequence. They were

allowed to dry in a clean room environment for a few hours and were subsequently kept at 85°C during 12 h.

The waveguide core material was synthesized in a similar way to the one reported in [13] and [15], based on hydrolysis and polycondensation of MAPTMS, to which zirconium(IV) propoxide (ZPO) mixed with methacrylic acid (MA) was added in a suitable molar proportion to attain the desired value of the refractive index. The precursor MAPTMS, diluted in ethanol, was first pre-hydrolyzed with acidic water (0.01 M HCl) in a water/MAPTMS molar ratio of 0.75 and stirred for 15 min. ZPO stabilized with MA and diluted with ethanol in molar ratios of 1:1:3, respectively, was stirred for 1 h and mixed with prehydrolyzed MAPTMS under vigorous stirring. Additional acidified water was added to the mixture until a water/MAPTMS molar ratio of 1.5 was achieved. After 30 min, the solution was filtered through a 0.2-μm filter and was ready for spin-coating deposition (using a procedure developed to achieve reproducible film thickness). Soda-lime glass substrates (refractive index of 1.513 at 632.8 nm) were employed, which had been previously cleaned through a standard cleaning sequence. The planar films were prebaked at 100°C for 30 min, to evaporate the residual solvent and avoid sticking when in contact with the photolithographic mask (lines from 4 μm to 24 μm, step 2 μm, $\pm$0.5 μm). The films were then exposed through the amplitude mask for about 30 s to the UV radiation of a 248-nm pulsed excimer laser; the fluence was 240 mJ/cm^2 and the pulse frequency was 10 Hz. The exposed samples were then soaked for a few minutes in ethanol for dissolution and removal of the unexposed material. After rinsing with pure water and drying, the samples with patterned ridge waveguides were post-baked at 130°C for 24 h. Finally, careful cleaving of both ends of the samples achieved the required optical interface quality for coupling the channel waveguides to optical fibers.

The refractive index and thickness of the hybrid glass films were usually evaluated employing a prism coupler setup, with a 0.6328-μm He-Ne laser. The refractive index of the hybrid glass material versus ZPO:MAPTMS ratio is shown in Figure 17; the 4:10 ratio was used in this work. Photoinscription of the channel waveguides by 248 nm irradiation

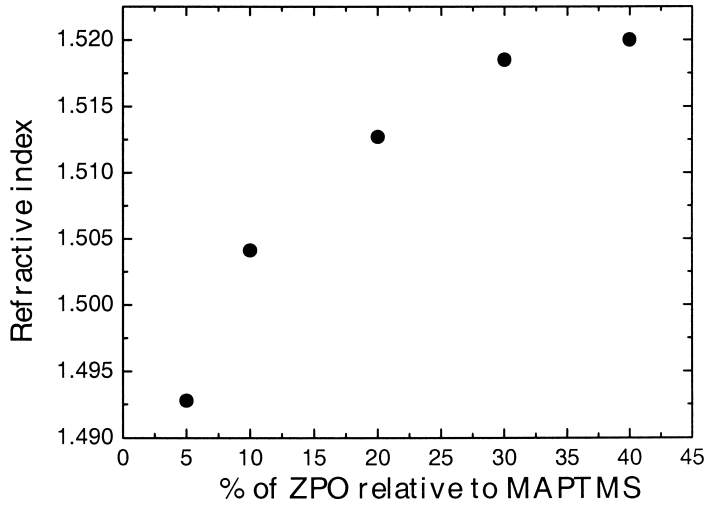

Figure 17. Refractive index of core planar films as a function of ZPO:MAPTMS percentage molar ratio.

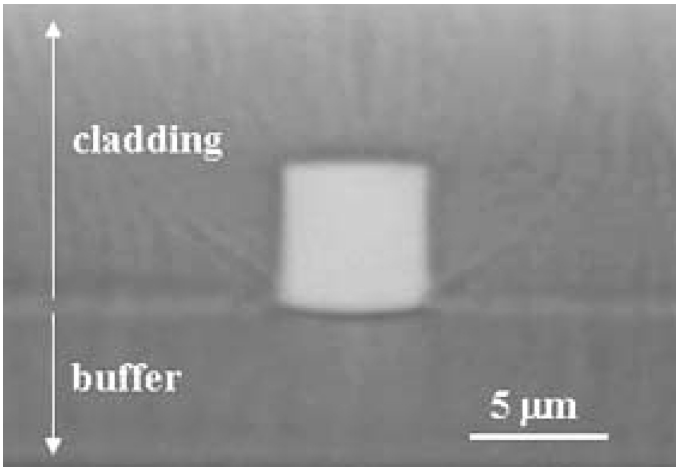

Figure 18. Microphotograph of the cross-section of buried channel waveguides fabricated on a silicon substrate.

requires a UV-transparent fused silica mask substrate. It was found that the hybrid material does not need the addition of any kind of photoinitiator to polymerize when exposed at this radiation wavelength, contrary to what happens when the exposure is performed using the 365-nm line of a mercury vapor lamp. The presence of a photoinitiator can be a drawback because of its potential contribution to the absorption loss of the final material at 1.55 μm. Good contact between the mask and the pre-baked hybrid film and optimized exposure parameters resulted in channels with perpendicular sidewalls, shown in Figure 18. Tolerances of film thickness of $\cong$0.2 μm, ridge waveguide width of $\cong$0.5 μm are typical. Surface roughness of planar films is usually below 5 nm; sidewalls roughness is below 50 nm, shown in Figure 19.

The channel waveguides were characterized in terms of absorption loss (400 to 1800 nm) using wide spectrum light coupled into multimode channel waveguides. The transmission absorption spectrum was measured with an optical spectrum analyzer and

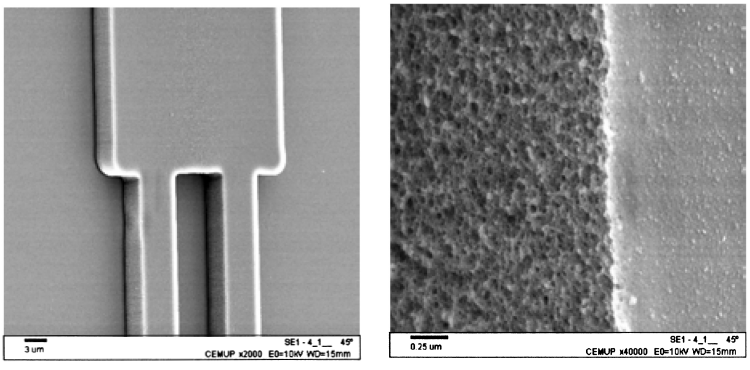

Figure 19. (a) Electron microscope top view of a device, (b) sidewall detail.

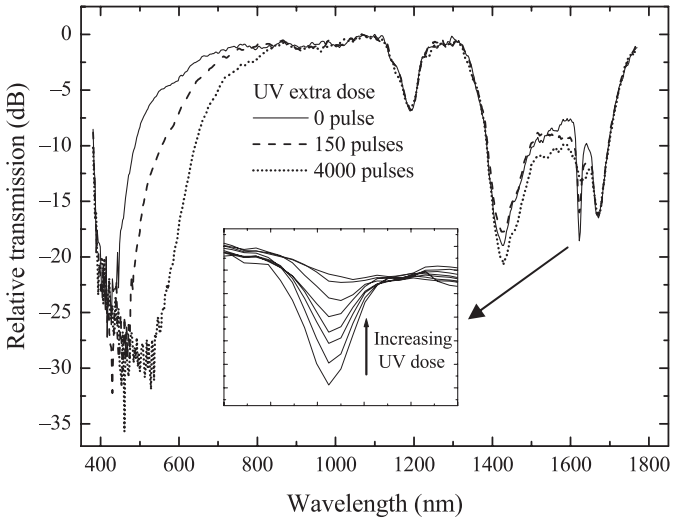

Figure 20. Relative transmission spectra of highly multimode channel waveguide for different UV post-exposure treatments. Inset shows detail illustrating bleaching of C=C double bonds.

normalized in terms of the white light source spectrum. Figure 20 presents the relative spectral attenuation of the propagating light in a 2.5-cm-long channel waveguide with $20 \times 6\ \mu m^2$ cross section. It is possible to identify an absorption band located at 1190 nm, which appears whenever the material contains organic components, due to the presence of C−H bonds.

The influence of the UV exposure dose on the transmission absorption spectrum of the hybrid material was studied using a double exposure method. In the first step, the UV dose was the minimum that allowed definition of a ridge waveguide with a good cross section, which corresponds approximately to 240 mJ/cm^2 at 10 Hz for 15 s. The ridge waveguide was subsequently re-exposed and the transmission spectra were registered, shown in Figure 20. As expected, the strength of the 1620-nm absorption band decreases with the exposure dose, indicating that the organic compound still polymerizes through the consumption of the C=C bonds.

In addition, waveguide and gratings can be produced in a single processing step, as described for the case of planar layers produced by flame hydrolysis deposition. However, in the case of hybrid sol-gel, the dissolution process leads to a corrugation grating as displayed in Figure 21. The transmission spectrum corresponding to the grating of Figure 21 is represented in Figure 22.

Conclusion

The photosensitive response of germanium-boron–doped silica obtained by flame hydrolysis deposition on oxidized silicon substrates was characterized in this study. The fabrication of devices using hybrid sol-gel technology using UV-assisted photopolymerization was described in detail. Additionally, demonstration of Bragg grating fabrication and direct writing of waveguides with a Bragg grating using the two different material systems was performed. This was a first step toward a practical method for mass production of elaborate devices avoiding dry-etch processing steps.

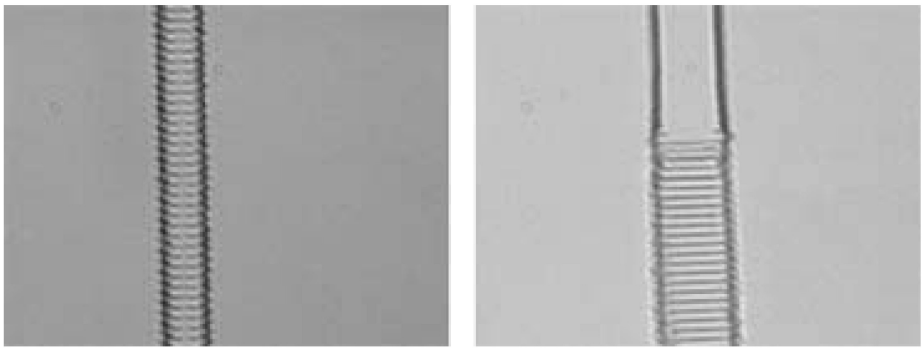

Figure 21. Microphotograph of channel waveguides fabricated in hybrid sol-gel after exposure through a combined mask of Figure 14 and dissolution of non-polymerized areas.

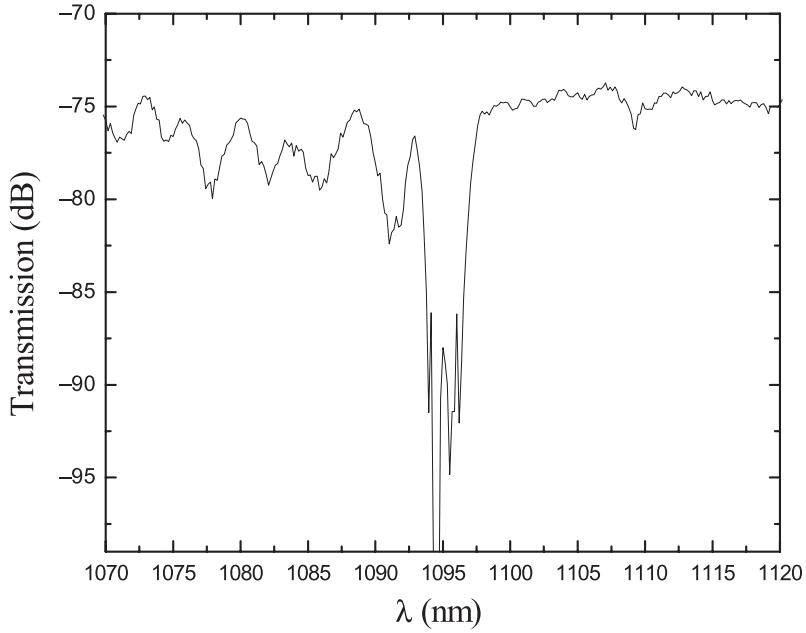

Figure 22. Transmission spectra of waveguide plus grating fabricated in hybrid sol-gel through a single exposure step.

Acknowledgment

This work was supported partially under project POCTI/ESE/43065/2001 and a Ph.D. fellowship SFRD/BD/4643/2001 awarded to P. J. Moreira, both with financial support of FCT–Fundação para a Ciência e a Tecnologia. This work was also partially supported by the European Project PLATON (PLAnar Technology for Optical Networks), action line IST-2002-4.8.3, contract number IST-2001-38168.

References

1. Kawachi, M., M. Yasu, and T. Edahiro. 1983. Fabrication of SiO_2–TiO_2 glass planar optical waveguides by flame hydrolysis deposition. *Electron. Lett*. 19(15):583.
2. Bonar, J. R., and J. S. Aitchison. 1996. Co-doping effects in rare earth doped planar waveguides. *Proc. IEE—Optoelectronics* 143:293.
3. Li, C. Y., J. Chisham, M. Andrews, S. I. Najafi, J. D. Mackenzie, and N. Peyghambarian. 1995. Sol-gel integrated optical coupler by ultraviolet light imprinting. *Electron. Lett*. 31:271.
4. Holmes, A. S., R. R. A. Syms, L. Ming, and M. Green. 1993. Fabrication of buried channel waveguides on silicon substrates using spin-on-glass. *Appl. Opt*. 32:4916.
5. Dong, L., J. L. Archambault, L. Reekie, and D. N. Payne. 1995. Photoinduced absorption change in germanosilicate performs: Evidence for the colour-center model of photosensitivity. *Appl. Opt*. 34:3436.
6. Etienne, P., P. Coudray, Y. Moreau, and J. Porque. 1998. Photocurable sol-gel coatings: Channel waveguides for use at 1.5 μm. *J. Sol-Gel Sci. Tech*. 13:523.
7. Mizrahi, V., P. J. Lemaire, T. Erdogan, W. A. Reed, and D. J. Digiovanni. 1993. Ultraviolet laser fabrication of ultrastrong optical fibre gratings and of germania-doped channel waveguides. *Appl. Phys. Lett*. 63(13):1727.
8. Maxwell, G. D., R. Kashyap, B. J. Ainslie, D. L. Williams, and J. R. Armitage. 1992. UV written 1.5 μm reflection filters in single mode planar silica guides. *Electron. Lett*. 28(22):2106.
9. Jarvis, R. A., J. D. Love, and F. Ladouceur. 1997. Bend-radius reduction in planar waveguides using UV post-tuning. *Electron. Lett*. 33(10):892.
10. Kashyap, R., G. D. Maxwell, and B. J. Ainslie. 1993. Laser-trimmed four-port bandpass filter fabricated in single-mode photosensitive Ge-doped planar waveguide, *IEEE Photon. Technol. Lett*. 5(2):191.
11. Maxwell, G. D., and B. J. Ainslie. 1995. Demonstration of directly written directional coupler using UV induced photosensitivity in a planar silica waveguide. *Electron. Lett*. 31(2):95.
12. Svalgaard, M. 1997. Direct writing of planar waveguide power splitters and directional couplers using a focused ultraviolet laser beam. *Electron. Lett*. 33(20):1694.
13. Najafi, S. I., T. Touam, R. Sara, M. P. Andrews, and M. A. Fardad. 1998. Sol-gel glass waveguide and grating on silicon. *IEEE J. Lightwave Technol*. 16:1640.
14. Coudray, P., P. Etienne, Y. Moreau, J. Porque, and S. I. Najafi. 1997. Sol-gel channel waveguide on silicon: Fast direct imprinting and low cost fabrication. *Opt. Commun*. 143:199.
15. Fardad, M. A., and M. Fallahi. 1998. Organic-inorganic materials for integrated optoelectronics. *Electron. Lett*. 34:1940.
16. Marques, P. V. S. 2000. Silica-on-silicon integrated optics by flame hydrolysis deposition. Ph.D. Thesis, University of Porto, Portugal.
17. Bilodeau, F., B. Malo, J. Albert, D. C. Johnson, K. O. Hill, Y. Hibino, M. Abe, and M. Kawachi. 1993. Photosensitization in optical fiber and silica on silicon/silica waveguides. *Opt. Lett*. 18(12):953.
18. Bonar, J., J. A. Bebbington, J. S. Aitchison, G. D. Maxwell, and B. J. Ainslie. 1995. Aerosol doped Nd planar waveguide laser. *Electron. Lett*. 31:99.
19. Zauner, D., K. Kulstad, J. Rathje, and M. Svalgaard. 1998. Directly UV-written silica-on-silicon planar waveguides with low insertion loss. *Electron. Lett*. 34(16):1582.

Biographies

Paulo V. S. Marques received a degree in physics (1991), an M.Sc in optoelectronics and lasers (1995), and a Ph.D. in physics (silica-on-silicon integrated optics by flame hydrolysis deposition, 2000), all from the University of Porto, Portugal. He is an assistant professor at the Faculty of Science, Porto University, and since July 2000 he has been developing research activity in the Optoelectronics and Electronics Systems

Unit of INESC PORTO, being responsible for several national and European research contracts. His current research interests include hybrid sol-gel–based waveguides, optical photosensitivity, Bragg gratings, electric-field poling, optical switching, and integrated optical sensors.

António A. M. P. Leite graduated in electrical engineering from the University of Porto, Portugal, in 1973. In 1979 he was awarded a Ph.D. from University College London, Department of Electronic and Electric Engineering, for research in holographic optical elements. Appointed associate professor at the Department of Physics, University of Porto, in 1979, he has been involved since then in projects on optical communication, fiber sensors, and integrated optic devices in lithium niobate, III-V semiconductors, polymers, and glass. His current interests are in the field of integrated optics (glass and polymer devices, electro-optic and rare-earth doped devices), fiber sensors, and sensor networks.

Paulo J. Moreira graduated in physics and applied mathematics and then concluded a Masters course in optoelectronics and lasers in the Physics Department of the University of Porto. He is currently a Ph.D. student working in the field of hybrid sol-gel for the development of integrated optic applications. His interests include microfabrication and nanotechnologies.

Miguel Melo was born in Porto, Portugal, in 1976. He graduated in optoelectronics and lasers from the University of Porto in 2001. He is now working as a researcher in the Optoelectronics and Electronic Systems Unit of INESC Porto. He is currently an M.Sc student in the Faculty of Engineering of the University of Porto.

Thomas E. A. Schmidt was born on December 11, 1975, in Wolfach, Germany. In 2002 he received his B.Sc. degree in Microsystems Technology from the University of Applied Sciences in Zweibruecken, Germany. Thereafter, he worked on position determination using miniaturized ultrasonic transducers at the University of Applied Sciences in Zweibruecken. In 2003 he joined the optoelectronics group at INESC Porto, where he is currently involved in developing thermo-optical switches using hybrid sol-gel technology. His research interests include microfabrication processes and MEMS.

Daniel Alexandre received a degree in electrical engineering (1999) from the University of Trás-os-Montes e Alto Douro and an M.Sc in optoelectronics and lasers (2003) from the University of Porto, Portugal. He is a teaching assistant at the University of Trás-os-Montes e Alto Douro and since 2002 he has been developing research in the Optoelectronics and Electronics Systems Unit of INESC PORTO. He is currently a Ph.D. student working in the field of laser direct writing for the development of integrated optic applications. His interests include microfabrication, laser direct writing, and integrated optical devices.

Roland Muenzner graduated in physics from the University of Tuebingen, Germany, in 1996, where he also obtained his doctorate in physics in 2001. Since the beginning of 2001 he has worked for Alcatel Research & Innovation at Stuttgart, Germany. There the focus of his research activities from 2001 to 2003 has been on passive integrated optical components, which has since switched to broadband wireless access systems.

J. Stewart Aitchison received a B.Sc. (with first class honors) and a Ph.D. from the Physics Department, Heriot-Watt University, Edinburgh, U.K., in 1984 and 1987 respectively. His dissertation research was on optical bistability in semiconductor waveguides. From 1988 to 1990 he was a Postdoctoral Member of Technical Staff at Bellcore, Red Bank, New Jersey. His research interests were in high nonlinearity glasses and spatial optical solitons. He then joined the Department of Electronics and Electrical Engineering, University of Glasgow, in 1990, and was promoted to a personal chair as professor of

photonics in 1999. His research was focused on the use of the half-band-gap nonlinearity of III-V semiconductors for the realization of all-optical switching devices and the study of spatial soliton effects. He also worked on the development of quasi-phase-matching techniques in III-V semiconductors, monolithic integration, optical rectification, and planar silica technology. His research group developed novel optical biosensors, waveguide lasers, and photosensitive direct writing processes based around the use of flame hydrolysis deposited (FHD) silica. In 1996 he was the holder of a Royal Society of Edinburgh Personal Fellowship and carried out research on spatial solitons as a visiting researcher at CREOL, University of Central Florida. He currently holds the Nortel Institute chair in Emerging Technology at the University of Toronto, Ontario, Canada. His research interests cover all-optical switching and signal processing, optoelectronic integration, and optical bio-sensors. His research has resulted in 7 patents, approximately 130 journal publications, and 200 conference publications. Dr. Aitchison is a member of the Optical Society of America, a senior member of the IEEE, and a Fellow of the Institute of Physics, London.